ACS Catalysis

Research Article

pubs.acs.org/acscatalysis

Silver Exchange of Layered Metal Oxides and Their Photocatalytic Activities

Jonathan Boltersdorf and Paul A. Maggard*

Department of Chemistry, North Carolina State University, Raleigh, North Carolina 27695-8204, United States

Supporting Information

ABSTRACT: Layered Dion–Jacobson phases $RbLaNb_2O_7$ and $RbA_2Nb_3O_{10}$ (A = Ca, Sr) and the Ruddlesden–Popper phase $Rb_2La_2Ti_3O_{10}$ were prepared by solid-state methods at a reaction time of 50 h and a temperature of 1100 °C. The products were silver-exchanged within a $AgNO_3$ flux at a reaction time of 24 h and a temperature of 250 °C. Substitution of silver cations into the interlayer spacing of the layered structures is found to decrease the optical bandgap sizes on average by ∼0.5 to ∼1.0 eV. The products were found by scanning electron microscopy (SEM) to exhibit irregularly shaped platelet morphologies with an average size of ∼1−5 μm across their lateral dimensions and stepped edges ranging from ∼20 to ∼300 nm in height. Significant increases in photocatalytic hydrogen production rates for all silver-exchanged products were observed. The silver-exchanged $RbA_2Nb_3O_{10}$ layered structures exhibited the highest photocatalytic hydrogen formation rates under ultraviolet and visible irradiation (∼13,616 μmol $H_2 \cdot g^{-1} \cdot h^{-1}$). These rates were 10 times higher than prior to silver exchange (∼1,418 μmol $H_2 \cdot g^{-1} \cdot h^{-1}$). However, photocatalytic activity under only visible light irradiation is not observed. It is also found that the silver cations located at the surfaces are reduced to Ag(s) after prolonged UV and visible light exposure in solution, which functions to increase their activity under UV irradiation. Electronic-structure calculations based on density functional theory show that the highest-energy valence band states are composed of Ag 4d-orbital and O 2p-orbital contributions within the interlayer spacing of the structure. The lowest-energy conduction band states arise from the Nb/Ti d-orbital and O 2p-orbital contributions that are confined to the two-dimensional niobate/titanate sheets within the structures and along which the excited-electrons can preferentially migrate.

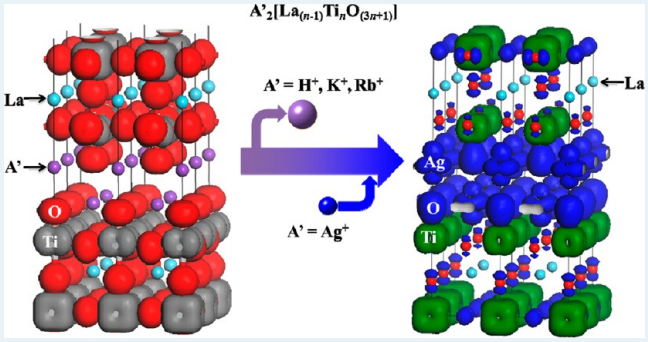

KEYWORDS: *photocatalysis, flux synthesis, layered-niobate, solar energy, band engineering*

INTRODUCTION

Growing energy concerns have led to an increased interest in metal oxide photocatalysts for conversion of solar energy to chemical fuels. Suspended metal oxide particles can absorb photons and function as photocatalysts for the production of hydrogen from water. In order for photochemical water splitting to occur, the conduction band edge of the metal oxide must be more negative than that of the proton reduction potential (0.0 V vs NHE at pH = 0), and the valence band edge must be more positive than the water oxidation potential (+1.23 V vs NHE at pH = 0).[1] Photocatalysts must efficiently absorb photons to produce electron–hole pairs that are separated and used to drive the water splitting redox reactions. Further, the metal oxide should exhibit prolonged stability upon irradiation in solution.[2] Currently, known metal oxide photocatalysts that are stable do not have sufficiently small bandgap sizes to absorb photons within the visible region, such as TiO_2, $SrTiO_3$, $NaTaO_3$, and $K_2La_2Ti_3O_{10}$.[1,3−5] There have been a growing number of recently reported approaches for tuning the properties of UV-active photocatalysts, such as using multiple transition metals, varying the particle morphologies, nanoscaling effects, combinatorial approaches, and band engineering of metal oxides.[6−13] The latter approach can be targeted via the low-temperature exchange of the interlayer cations with transition metal cations, e.g., those with d^{10} electron configurations (Ag(I) or Cu(I)).[9,13−17] Transition metals with filled d-orbitals can increase the valence-band energy and thus decrease the bandgap size into the visible region.[9,18] Further, metal oxides with layered structures are among the most active photocatalysts for splitting water into H_2 and O_2 under UV light irradiation, including $HCa_2Nb_3O_{10}$, $K_4Nb_6O_{17}$, and $La_2Ti_2O_7$.[1,14,19] Comparisons among layered perovskite structures with variable layer thicknesses and interlayer cations are promising for providing a deeper understanding and optimization of their photocatalytic properties.

The layered Dion–Jacobson phases have the general formula $A'[A_{(n-1)}B_nX_{(3n+1)}]$, while that for the Ruddlesden–Popper (RP) series is $A_2'[A_{(n-1)}B_nX_{(3n+1)}]$ (A′ = Rb, Ag; A = Ca, Sr, La; B = Nb, Ti; X = O), where A′ is the interlayer cation and n

Received: June 19, 2013
Revised: September 24, 2013
Published: September 27, 2013

defines the B-cation octahedral layer thickness (n = 2, 3). Both types of phases exhibit significant ion exchange of their interlayer cations. Exchange reactions can occur without alteration of adjacent metal oxide layers, with the structures differing only in their interlayer separations.[13,15,16,20−24] Herein, silver exchange reactions were performed using a low-temperature $AgNO_3$ flux. The $Rb_2La_2Ti_3O_{10}$, $RbLaNb_2O_7$, and $RbA_2Nb_3O_{10}$ (A = Ca, Sr) phases were selected as starting materials because their structures and properties have previously been studied in detail.[3,9,13,14,25−28] All products were characterized by powder X-ray diffraction, UV−vis diffuse reflectance spectroscopy, Brunauer−Emmet−Teller surface area analysis, field emission scanning electron microscopy, and energy dispersive X-ray spectroscopy in order to investigate the effects of silver exchange on their optical, electronic, and photocatalytic properties. Electronic structure calculations were used in order to probe the influence of the Ag 4d-orbital contributions on the bandgap size and photocatalytic hydrogen production of these layered metal oxides.

METHODS

Synthesis. $Ag_2La_2Ti_3O_{10}$ was prepared by a low temperature ion-exchange reaction using solid-state prepared $Rb_2La_2Ti_3O_{10}$ and $AgNO_3$. The solid-state synthesis of $Rb_2La_2Ti_3O_{10}$ was performed by combining a stoichiometric mixture of reagent grade Rb_2CO_3 (Alfa Aesar, 99.9%; 25% excess for volatilization), La_2O_3 (Alfa Aesar, 99.9%; preheated and dried at 900 °C), and TiO_2 (Alfa Aesar, 99.9%), grinding, pelletizing, and heating in an alumina crucible for 50 h at 1100 °C inside a box furnace.[28] The products were radiatively cooled to room temperature inside the box furnace. The ion-exchange reaction was carried out by mixing ground $Rb_2La_2Ti_3O_{10}$ powders with $AgNO_3$ (Alfa Aesar, 99.9%) in a 1:4 molar ratio ($Rb_2La_2Ti_3O_{10}/AgNO_3$) and heating in an alumina crucible inside a box furnace for 24 h at 250 °C. Excess $AgNO_3$ for all flux exchanged products was removed by washing and centrifuging with deionized water.

$AgLaNb_2O_7$ was prepared by a low temperature ion-exchange reaction using solid-state prepared $RbLaNb_2O_7$ and $AgNO_3$. The solid-state synthesis of $RbLaNb_2O_7$ was performed according to reported literature procedures, which involved grinding, pelletizing, and heating a stoichiometric mixture of reagent-grade Rb_2CO_3 (Alfa Aesar, 99%; 25% excess for volatilization), La_2O_3 (Alfa Aesar, 99.9%, preheated and dried at 900 °C), and Nb_2O_5 (Alfa Aesar, 99.9985%) in an alumina crucible for 50 h at 1100 °C inside a box furnace.[13,28] The products were radiatively cooled to room temperature. The ion-exchange reaction was carried out by mixing ground $RbLaNb_2O_7$ powders with $AgNO_3$ (Alfa Aesar, 99.9%) in a 1:4 molar ratio ($RbLaNb_2O_7/AgNO_3$) and heating for 24 h at 250 °C.

The $AgA_2Nb_3O_{10}$ (A = Ca, Sr) phases were prepared by a low temperature ion-exchange reaction using solid-state prepared $RbA_2Nb_3O_{10}$ and $AgNO_3$. The solid-state synthesis of $RbA_2Nb_3O_{10}$ was performed according to literature procedures by combining a stoichiometric mixture of reagent grade Rb_2CO_3 (25% excess for volatilization), ACO_3 (Alfa Aesar, 99.99%), and Nb_2O_5, grinding, pelletizing, and heating in an alumina crucible for 50 h at 1100 °C inside a box furnace.[29,30] The products were radiatively cooled to room temperature inside the box furnace. The ion-exchange reaction was carried out by mixing ground $RbA_2Nb_3O_{10}$ powders with $AgNO_3$ in a 1:4 molar ratio ($RbA_2Nb_3O_{10}/AgNO_3$) and heating in an alumina crucible inside a box furnace for 24 h at 250 °C. Fine homogeneous gray-colored powders of $AgA_2Nb_3O_{10}$ were obtained and characterized by powder X-ray diffraction.

Characterization. The products were characterized by high-resolution powder X-ray diffraction (PXRD) on an INEL diffractometer using Cu Kα_1 (λ = 1.54056 Å) radiation from a sealed-tube X-ray generator (35 kV, 30 mA) using a curved position sensitive detector (CPS120), as well as on a Rigaku R-Axis Spider with a curved image-plate detector. Field-emission scanning electron microscopy (FESEM) analyses were performed on a JEOL SEM 6400. Energy-dispersive X-ray spectroscopy (EDX) was performed on a 4Pi Isis EDX system attached to a Hitachi S3200 variable pressure scanning electron microscope (VPSEM) for image acquisition and elemental analysis. Lattice parameters of the solid-state prepared samples were refined using the JADE 9 software and were found to be consistent with the literature values.[9,15,16,30−33] The BET specific surface area analyses were performed using a Quantachrome ChemBET Pulsar TPR/TPD with N_2 utilized as the adsorbate. UV−vis diffuse reflectance spectra (DRS) were collected on a Shimadzu UV-3600 equipped with an integrating sphere. Pressed barium sulfate powder was used as a reference, and the data were transformed using the Kubelka−Munk function ($F(R)$) and plotted as Tauc plots of $(F(R) \times h\nu)^n$ vs $h\nu$ (eV) to obtain direct (n = 2) and indirect (n = 1/2) bandgap sizes.[34]

Photocatalysis Measurements. Photocatalytic rates of hydrogen production were measured for all samples using an outer-irradiation type fused-silica reaction cell with a volume of 70 mL and irradiated under ultraviolet light (λ > 230 nm) and visible light (λ > 420 nm). Each sample was loaded with a 1 wt % platinum cocatalyst as a kinetic aid for reduction of water to hydrogen using the photochemical deposition method (PCD).[6] The PCD method was conducted using 150 mg of each sample and 30 mL of an aqueous solution of dihydrogen hexachloroplatinate (IV) ($H_2PtCl_6{\cdot}6H_20$; Alfa Aesar, 99.95%) irradiated for 2 h using a 400 W Xe arc lamp with constant stirring using a magnetic stir bar. Methanol (~2 mL) was added to each vessel prior to irradiation to aid in control of Pt dispersion and to serve as an organic sacrificial agent.[35] After platinization, the particles were washed and centrifuged with deionized water to remove any excess Cl^- ions and dried overnight in an oven at 80 °C.

Photocatalytic hydrogen production measurements were conducted with 50 mg of the platinized samples in a fused-silica reaction vessel filled with a 20% aqueous methanol solution. Methanol functions as a hole scavenger, photo-oxidizing to CO_2, and allows for the measurement of H_2 production without the potentially rate-limiting step of oxidation of water to O_2.[36] The particle suspension was degassed by stirring in the dark while purging with N_2 for 30 min. The reaction cell was irradiated for 6−8 h using an external 1000 W Xe arc lamp equipped with an IR water filter and cooled with an external fan; an additional visible filter (>420 nm) was used for visible light phototesting. The outlet of the reaction vessel was connected to a horizontal quartz tube with a moveable liquid bubble, allowing volumetric determination of evolved gases at constant pressure. Progress of the photocatalytic reactions were recorded at 30 min intervals and used for calculations of the amount of evolved gases generated in μmol $H_2{\cdot}g^{-1}{\cdot}h^{-1}$ and quantified with a gas chromatograph

equipped with a thermal conductivity detector (TCD) to detect H_2 and CO_2 products.

Electronic Structure Calculations. Electronic structure calculations were performed on the geometry-optimized structures of $A_2'La_2Ti_3O_{10}$ (A′ = Rb, Ag) using CASTEP, a density functional theory (DFT) software package using a plane-wave basis set.[37] The Perdew−Burke−Ernzerhof (PBE) functional in the generalized gradient approximation (GGA) and ultrasoft core potentials were utilized in the calculations of the electronic band structures, partial densities of states, and electron density plots.[38]

RESULTS AND DISCUSSION

Synthesis and Structural Description. The layered $Rb_2La_2Ti_3O_{10}$ and its silver-exchanged analogue, $Ag_2La_2Ti_3O_{10}$, have been reported in the literature in both hydrated and anhydrous forms. The structure is composed of a triple layer of condensed TiO_6 octahedra separated by a double layer of rubidium or silver cations. The cations within the interlayer spacing pack in a distorted rock-salt type arrangement through the apical oxygen atoms of the TiO_6 triple layers.[13] These metal oxides are hygroscopic owing to the solvation of the interlayer cations. This results in an increase in the interlayer spacing along the *c*-axis and a higher reactivity for water splitting.[16,39] The $RbLaNb_2O_7$ is a layered perovskite that crystallizes in an orthorhombic space group and contains double layers of NbO_6 octahedra separated by a single layer of rubidium cations in the interlayer spacing, as described previously.[15,14] Following silver exchange, the $AgLaNb_2O_7$ phase crystallizes in the tetragonal space group.[9] The $AgLaNb_2O_7$ phase cannot directly be prepared by solid-state methods but can be synthesized by flux exchange of $RbLaNb_2O_7$.[9,33]

The layered perovskite structure of $RbA_2Nb_3O_{10}$ (A = Ca, Sr) consists of triple layers of NbO_6 octahedra separated by a single layer of rubidium cations in the interlayer spacing. Larger interstitial cation sizes (Ca, Sr) increase the *c*-axis parameter, as found here in comparing the lattice parameters of $RbCa_2Nb_3O_{10}$ (c = 14.9743(5) Å) and $RbSr_2Nb_3O_{10}$ (c = 15.3170(2) Å).[30] The silver exchange products of the $RbA_2Nb_3O_{10}$ structures have not been previously reported in the literature and were accomplished with no residual Rb in the structure, as confirmed by EDX spectroscopy in the Supporting Information. The X-ray powder pattern of the Ca-analogue exhibits a lower degree of crystallinity. The powder X-ray patterns do not show simple shifting in the peak positions that would result from ion-exchange of the interlayer cations but instead show new unidentified patterns. Related work by Woodward et al.[40] has shown silver exchange of $Li_2[A_{1.5}Nb_3O_{10}]$ precursors produces the layered $Ag_{1.1}Ca_{0.9}[Ca_{0.6}Ag_{0.9}Nb_3O_{10}]$ phase, in which Ag(I) ions occupy both the A and A′ sites of the RP structure. The silver exchange products of the $RbA_2Nb_3O_{10}$ structures are related to the layered $Ag_{1.1}Ca_{0.9}[Ca_{0.6}Ag_{0.9}Nb_3O_{10}]$ phase, judging from similarities of their PXRD patterns. The full structural details of these silver-exchanged layered phases have yet to be determined.

Interlayer cations in these layered metal oxides have been shown to exhibit varied coordination numbers and geometries based on crystal radii, thus impacting the overall structure and crystal symmetry. It has been shown that $RbCa_2Nb_3O_{10}$ (*P*4/*mmm*) crystallizes in a tetragonal space group with intercalated eight-coordinate Rb cations, while $KCa_2Nb_3O_{10}$ (*Cmcm*; $P2_1/m$) crystallizes in an orthorhombic or monoclinic space group with intercalated six-coordinate potassium cations. The size and lower coordination number of the smaller interlayer cation can cause octahedral tilting and other distortions to the NbO_6 octahedra layers.[41] Rubidium cations (166−175 pm) exhibit a greater crystal radii than that of the silver cations (114−129 pm).[42] The unidentified silver-exchanged phase may possess a different local coordination like that of potassium, and perhaps distorting the tetragonal system to one of lower symmetry.

Particle Morphologies and Sizes. Solid-state prepared $Rb_2La_2Ti_3O_{10}$ and flux-exchanged $Ag_2La_2Ti_3O_{10}$ particle morphologies and sizes were characterized by FESEM, shown in Figure 1. The particles varied in size across their lateral dimensions (~0.3−5 μm) and formed together in aggregates with irregularly shaped platelet morphologies and stepped edges. The layers in both were much thicker than other rubidium-containing particles with larger stepped edges (~200−700 nm). The edges and corners of each layer of the $Ag_2La_2Ti_3O_{10}$ particles were covered in nanosized fibrous growths (~20−115 nm). The PXRD data did not detect any impurities present in the sample before photocatalytic hydrogen generation measurements.

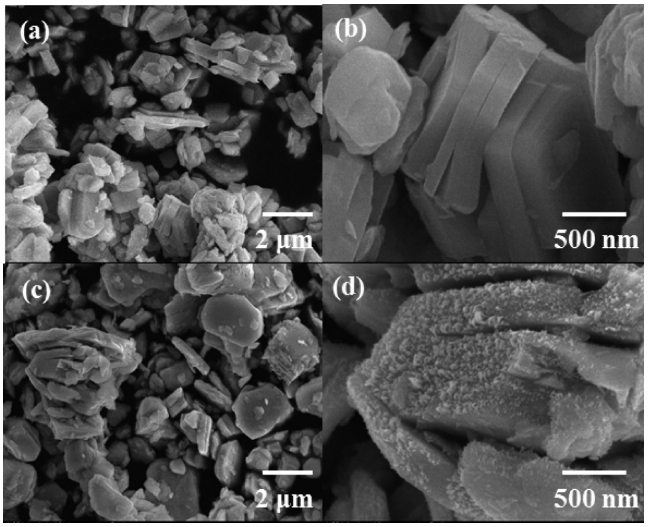

Figure 1. FESEM images of solid-state prepared $Rb_2La_2Ti_3O_{10}$ (a and b) and silver-exchanged $Ag_2La_2Ti_3O_{10}$ (c and d).

The platelet-shaped sizes and particle morphologies of solid-state prepared $RbLaNb_2O_7$ and silver-exchanged $AgLaNb_2O_7$ have been previously reported in the literature.[9] These double-layered perovskites appear to exhibit a layer-by-layer growth that results in stepped edges over the platelet particles and over which platinum preferentially photodeposits on the surfaces. Similar rounded-platelet morphologies are observed for both phases. These platelet particles exhibit thicknesses of ~100−300 nm and lateral dimensions of ~1−6 μm, with stepped edges of ~20−100 nm in height.[9]

The $RbA_2Nb_3O_{10}$ (A = Ca, Sr) and silver-exchanged products were characterized by FESEM, as shown in Figures 2 and 3. Overall particle sizes varied for $RbCa_2Nb_3O_{10}$ (~2−16 μm) and $RbSr_2Nb_3O_{10}$ (~0.6−4.5 μm), as measured across their lateral dimensions. Aggregates of irregularly shaped platelets with stepped corners and edges (~17−190 nm) were observed for both. The $RbA_2Nb_3O_{10}$ structures exhibited smoother edges and well-defined layers that showed characteristics of a layer-by-layer particle growth as seen for the

dx.doi.org/10.1021/cs400466b | ACS Catal. 2013, 3, 2547−2555

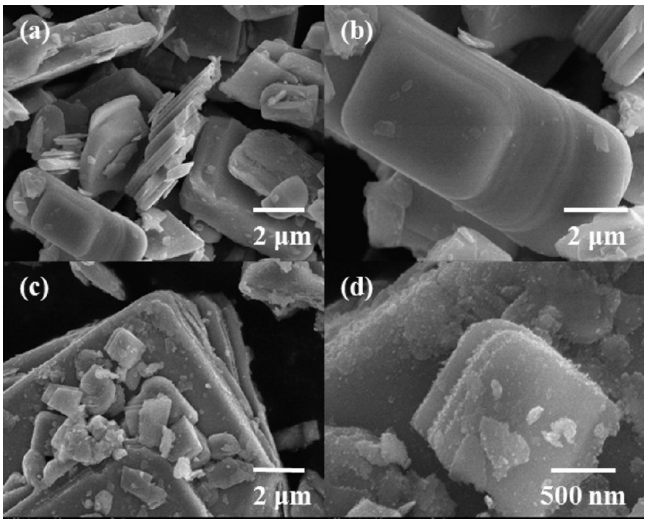

Figure 2. FESEM images of solid-state prepared $RbCa_2Nb_3O_{10}$ (a and b) and after silver exchange (c and d).

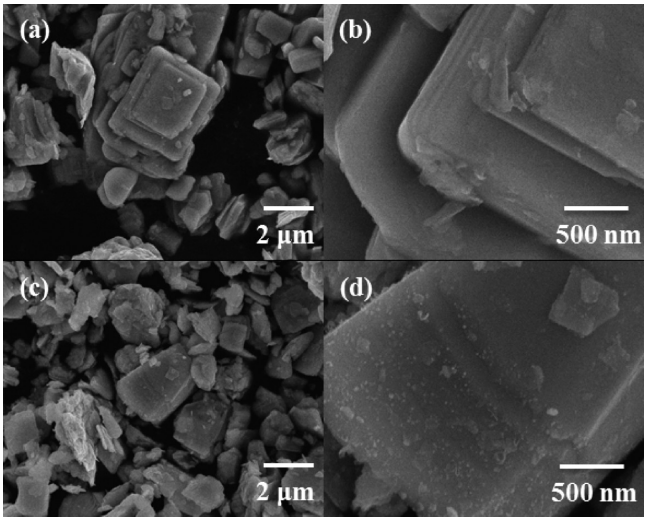

Figure 3. FESEM images of solid-state prepared $RbSr_2Nb_3O_{10}$ (a and b) and after silver exchange (c and d).

$RbLaNb_2O_7$ particles.[9] The silver-exchanged products exhibited thicker layers (~1.5−2 μm) with silver-rich sites on the surfaces of the irregular-platelets, concentrated primarily on the edges and corners (~80 nm) of the layers. Particle sizes of the silver-exchanged $AgCa_2Nb_3O_{10}$ and $AgSr_2Nb_3O_{10}$ were more regular, averaging between ~3−5 μm and ~1−3 μm, respectively. Thus, the particle characteristics were maintained after a low-temperature silver exchange. Bulk elemental analyses of the $AgA_2Nb_3O_{10}$ silver-exchanged products show complete ion exchange with no residual rubidium within the interlayer spacings. Elemental analyses of the particulates on the particles' surfaces show these to be silver-richer in comparison to the flat smooth surfaces. The PXRD data of the silver-exchanged products show no silver metal or $AgNO_3$ present. The EDX data of the silver-exchanged layered structure showed a 1:3 ratio of the atomic percent between the silver and niobium, as expected for a "$AgA_2Nb_3O_{10}$" composition.

Optical Properties and Electronic Structure Calculations. Layered metal oxides can function as efficient photocatalysts for hydrogen production when irradiated by photons with energy greater than their bandgap sizes. Light absorption causes excitation of electrons between the valence and conduction bands, and these electron−hole pairs can then be separated within the space charge region near the particle's surfaces. Electrons in the conduction band migrate across the potential gradient within the space charge region, arriving at the surfaces, and can then reduce adsorbed water to H_2. The holes generated within the valence band are filled by the oxidation of methanol to CO_2 or as well, by the oxidation of water.[1,9,43] On layered metal oxides there is typically a physical separation of the reduction and oxidation sites over different surface sites.[27]

The optical bandgap sizes (E_g) of the layered oxides were calculated from the onset of absorption obtained from diffuse reflectance data. Direct and indirect band gap transitions were determined from Tauc plots of $(F(R) \times h\nu)^n$ versus $h\nu$ (eV), shown in Figure 4 and listed in Table 1, where $n = 2$ and $n = 1/2$ for direct and indirect transitions, respectively.[9,14,28,34] The bandgap sizes were measured for all Rb-containing layered oxides (~3.10−3.60 eV) and the silver-exchanged products (~2.40−2.85 eV), each showing a red shift in the bandgap size of ~0.5−1.0 eV upon exchange for silver cations. The red shift in all silver-exchanged products reduced the optical bandgap sizes into the visible region. The smallest bandgap size observed was for $Ag_2La_2Ti_3O_{10}$ (~2.40 eV), a Ruddlesden−Popper phase that has a larger silver content in the interlayer spaces that consist of a double layer of silver cations. Thus, the layered oxide with the greatest silver content should result in increased Ag(I) d^{10}-orbital contributions to the top of the valence band.

Electronic structure calculations were performed on the geometry-optimized structures of $A_2'La_2Ti_3O_{10}$ (A′ = Rb, Ag) using CASTEP. The band structures and electron density plots of all silver-exchanged layered oxides shared similar features in terms of the atomic contributions to the uppermost valence-band and lowermost conduction-band states, as shown in Figures 5 and 6 for $Ag_2La_2Ti_3O_{10}$. Contributions to the valence and conduction bands are projected out in the partial densities of states, with the electron density at the band edges projected out to the left. The highest-energy valence band states are composed of Ag 4d and O 2p orbital contributions within the interlayer spacings. The Ag 4d contribution to the valence band for the $Ag_2La_2Ti_3O_{10}$ structure reduces the bandgap size in comparison to the rubidium-containing layered structures. The lowest-energy conduction band states are composed of Ti 3d orbitals within the triple titanate layers of the layered perovskite structure.

The electronic band structure diagram is plotted in Figure 6, with labels for the direct and indirect band gap transitions. A direct band gap transition involves excitation of electrons at a common k-point, e.g., at the Γ point. The indirect band gap transition is between two different *k*-points, e.g., between the R and Γ point for the valence and conduction bands, respectively. The relatively higher charge-carrier mobility within the niobate/titanate sheets is confirmed by the larger band dispersion of the conduction bands in directions along these two-dimensional layers. By contrast, the band dispersion is relatively flat between directions perpendicular to the niobate/titanate sheets, i.e., along the *c*-axis. These flat bands are indicative of lower charge carrier mobility along the *c*-axis direction.[9]

Photocatalytic Properties. The photochemical deposition of Pt islands on the surfaces of layered metal oxides has been shown to function as a cocatalyst for hydrogen evolution. The platinum nanoparticles on the surfaces induce a potential

dx.doi.org/10.1021/cs400466b | *ACS Catal.* 2013, 3, 2547−2555

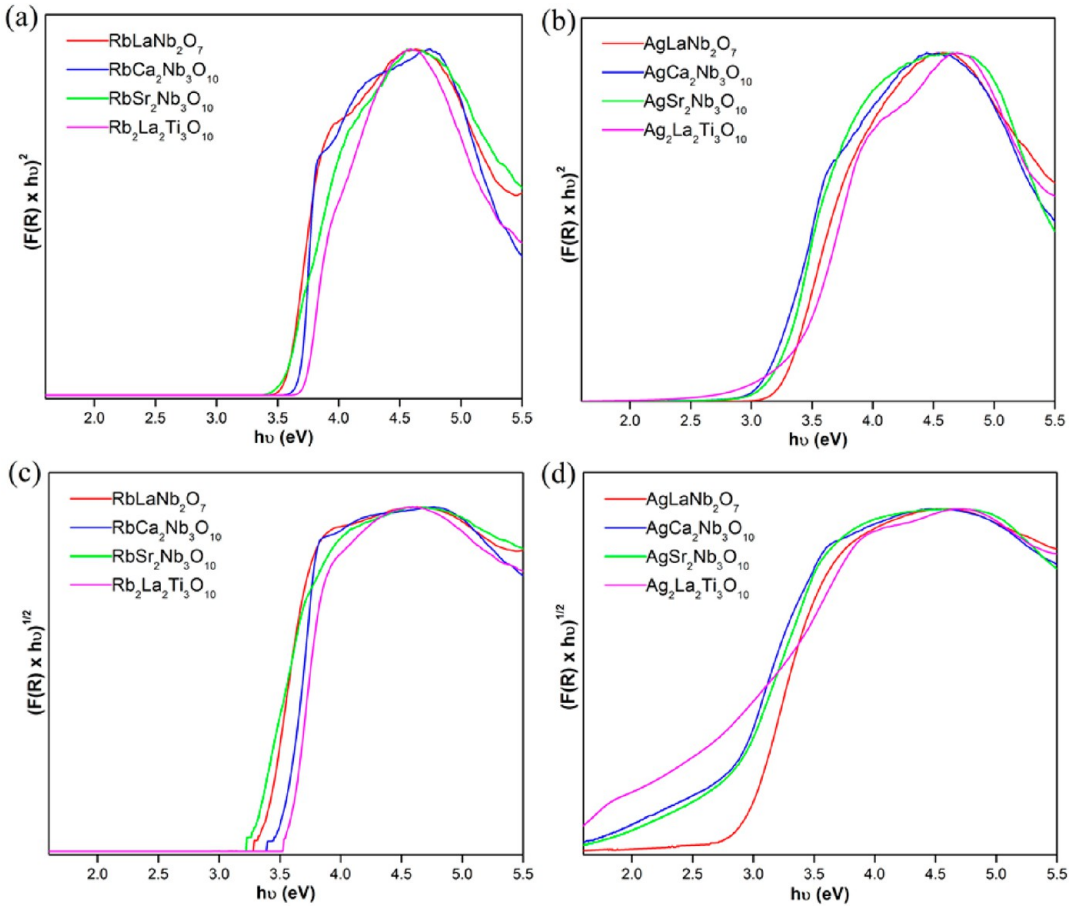

Figure 4. UV−vis diffuse reflectance spectra plotted as Tauc plots of $(F(R) \times h\nu)^n$ vs $h\nu$ (eV) for direct (n = 2) and indirect (n = 1/2) bandgap transitions of (a, c) rubidium-containing perovskites and (b, d) the silver-exchanged products, respectively.

Table 1. BET Specific Surface Area Analyses and Photocatalytic Rates of Hydrogen Production under UV and Visible Light (λ > 230 nm) Irradiation. Direct (n = 2) and Indirect (n = 1/2) Band Gaps Were Obtained from Tauc Plots of $(F(R) \times h\nu)^n$ vs $h\nu$ (eV).

		band gap transitions (eV)			UV activity[b] (μmol $H_2 \cdot g^{-1} \cdot h^{-1}$)	
sample	specific surface area ($m^2 \cdot g^{-1}$)	direct	indirect	turnover[a] (μmol H_2/μmol catalyst)	with Pt	without Pt
$RbLaNb_2O_7$	1.5	3.50	3.30	1.0	331	
$AgLaNb_2O_7$	4.2	3.20	2.85	5.1	1445	208
$RbCa_2Nb_3O_{10}$	1.9	3.70	3.50	6.0	1418	
"$AgCa_2Nb_3O_{10}$"	2.1	3.00	2.65	51	13616	2030
$RbSr_2Nb_3O_{10}$	2.7	3.50	3.10	8.0	1929	
"$AgSr_2Nb_3O_{10}$"	3.0	3.10	2.66	14	3265	1256
$Rb_2La_2Ti_3O_{10}$	2.3	3.70	3.60	19	3618	
$Ag_2La_2Ti_3O_{10}$	3.1	3.10	2.40	3.6	763	230

[a]Turnover number calculated for samples under UV irradiation with Pt cocatalysts. [b]Photocatalytic conditions: outer irradiation 1000 W high-pressure Xe arc lamp, 50 mg product, 20% methanol solution (N_2 purged) and measured over a period of 6 h.

gradient in which excited electrons can transfer from the metal oxide to the Pt(s). A uniform and preferential deposition of Pt(s) has been previously reported, with the number of Pt deposits found to increase with an increase in the amount of loading until optimal conditions are reached.[44,45] Previous results have shown that Pt deposits can be used to map the active sites of a layered oxide surface, with stepped features at the layers being the preferred deposition sites.[9,43,46]

Photocatalytic hydrogen production rates were measured for each layered metal oxide under UV and visible light irradiation for both the Rb- and Ag-analogues, shown in Table 1 and Figure 7. Turnover numbers for all phases measured under UV irradiation over a period of 6 h were greater than unity. The highest observed UV activity for the Rb-containing perovskites was for $Rb_2La_2Ti_3O_{10}$ (~3,618 μmol $H_2 \cdot g^{-1} \cdot h^{-1}$). High rates of hydrogen formation for $Rb_2La_2Ti_3O_{10}$ can be attributed to the hydration and expansion of its interlayer spacings. Dion−Jacobson layered perovskites commonly exhibit this hydration that facilitates the increased migration of water and methanol through the interlayer spacing.[14,33,39] The silver-exchanged $AgA_2Nb_3O_{10}$ layered structures exhibited the highest photocatalytic hydrogen formation rates measured in aqueous

dx.doi.org/10.1021/cs400466b | ACS Catal. 2013, 3, 2547−2555

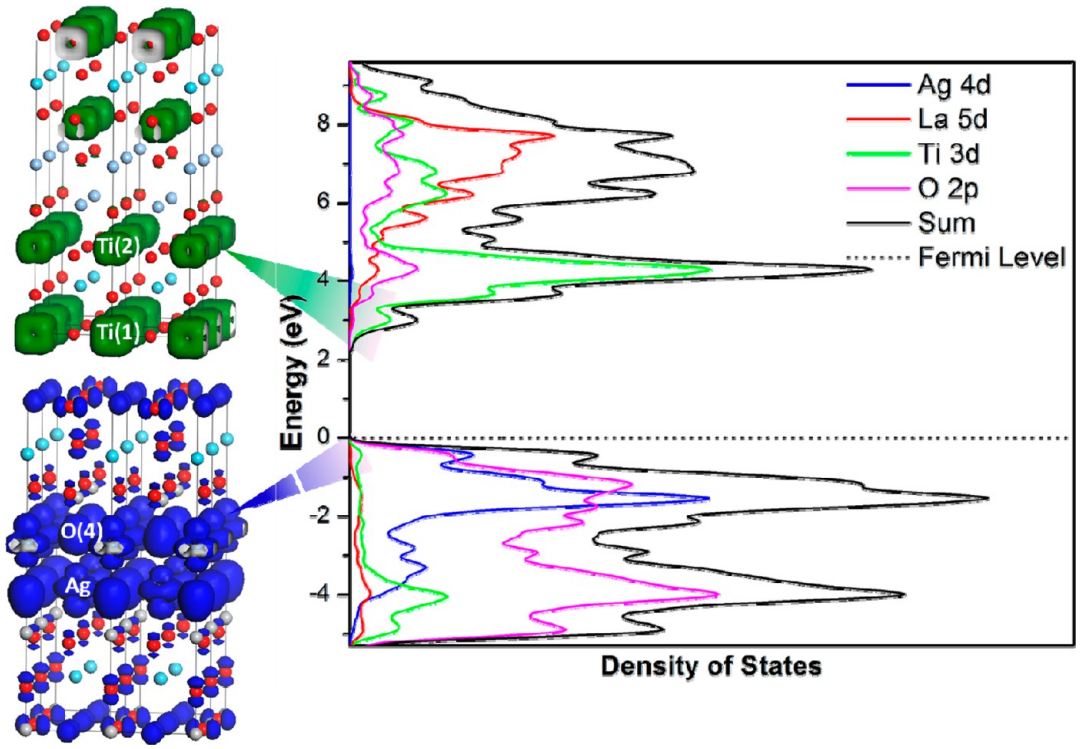

Figure 5. Density of states diagram (right) and electron density plot (left) of $Ag_2La_2Ti_3O_{10}$ that shows electron density in the bottom of the conduction band (green) and the top of the valence band (blue). The electron density plot for the structure of $Ag_2La_2Ti_3O_{10}$ is shown to the left with silver (gray), lanthanum (blue), titanium (white), and oxygen (red) spheres.

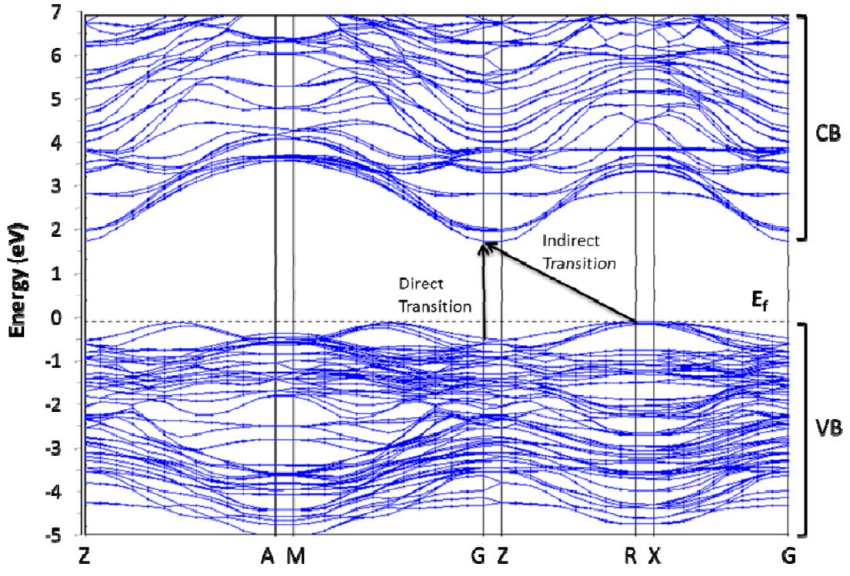

Figure 6. Band structure for $Ag_2La_2Ti_3O_{10}$ with the direct (n = 2) and indirect (n = 1/2) band gap transitions shown at the Γ point and from the R to Γ point in reciprocal space, respectively.

methanol under ultraviolet irradiation (~13,616 μmol $H_2 \cdot g^{-1} \cdot h^{-1}$). These rates were 10 times higher than before silver exchange (~1,418 μmol $H_2 \cdot g^{-1} \cdot h^{-1}$). A decrease in the optical bandgap size and an increase in surface area for the silver-exchanged layered structures act to enhance UV activity. An increase in the surface area increases the amount of potential active sites on the surfaces of a bulk sample. Only $Ag_2La_2Ti_3O_{10}$ exhibited lower photocatalytic activity under UV light irradiation after silver exchange, perhaps owing to the large amount of fibrous growths coating its surfaces, as described earlier.

Photocatalytic H_2 rates were compared to the most commonly studied metal oxides in the literature, e.g., TiO_2, $La_2Ti_2O_7$, and $MTaO_3$ (M = Li, Na, K).[1,4,6,11,19,47] TiO_2 with a Pt cocatalyst and $La_2Ti_2O_7$ with a NiO cocatalyst has been reported to yield ~947 μmol $H_2 \cdot g^{-1} \cdot h^{-1}$ and ~441 μmol $H_2 \cdot g^{-1} \cdot h^{-1}$, respectively. $MTaO_3$ (M = Li, Na, K) and La-doped $NaTaO_3$ with a NiO cocatalyst was reported to generate ~3.39 and ~19.8 mmol $H_2 \cdot g^{-1} \cdot h^{-1}$, respectively.[1] By comparison, the

dx.doi.org/10.1021/cs400466b | ACS Catal. 2013, 3, 2547−2555

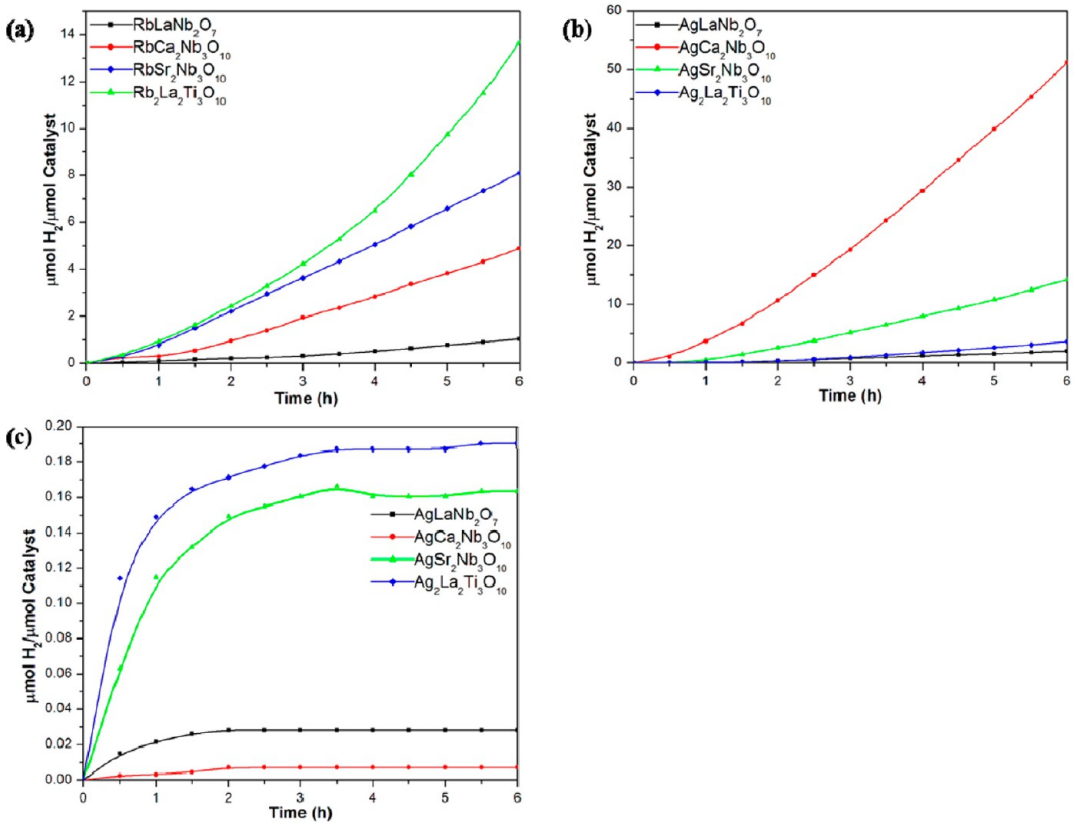

Figure 7. Photocatalytic hydrogen production (μmol H_2/μmol catalyst) versus time (h) for (a) rubidium-containing perovskites prepared by solid-state methods and silver-exchanged perovskites under (b) UV (λ > 230 nm) and (c) visible light (λ > 420 nm) irradiation.

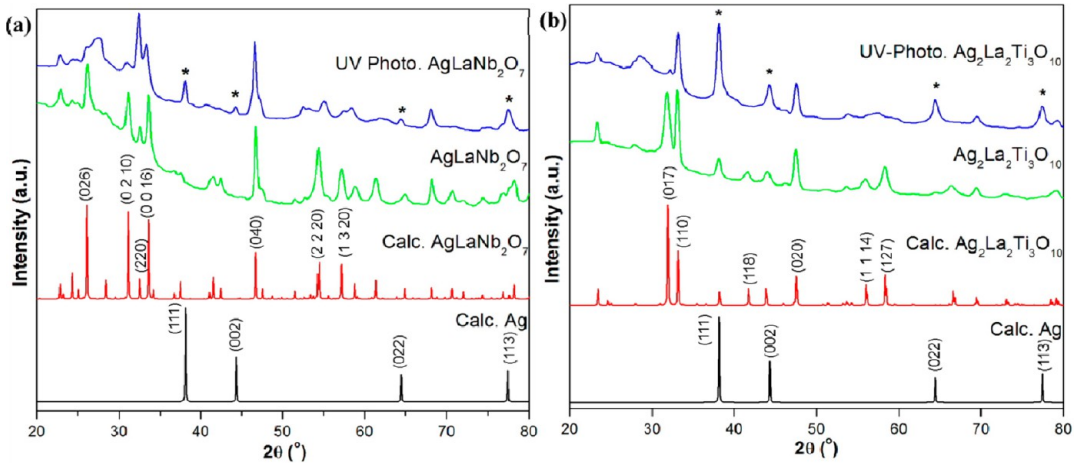

Figure 8. PXRD of silver-exchanged layered perovskites before and after phototesting for 7 h under UV irradiation for (a) $AgLaNb_2O_7$ and (b) $Ag_2La_2Ti_3O_{10}$. The asterisked peaks label the Ag(s).

Rb-containing layered perovskites loaded with Pt cocatalysts yielded ~331−3,618 μmol $H_2 \cdot g^{-1} \cdot h^{-1}$, while platinized silver-exchanged phases yielded ~763−13,616 μmol $H_2 \cdot g^{-1} \cdot h^{-1}$. Photocatalytic H_2 production measurements of the silver-exchanged phases without Pt cocatalysts were also obtained. Initial H_2 evolution rates under UV irradiation were comparatively low, but H_2 generation greatly increased after the photochemical reduction of silver. The photocatalytic rates for all silver-exchanged phases were less than those with Pt cocatalysts. Without Pt cocatalysts, the silver-exchanged phases generated ~208−2,030 μmol $H_2 \cdot g^{-1} \cdot h^{-1}$; $AgCa_2Nb_3O_{10}$ had the highest photocatalytic rate with or without Pt cocatalysts.

The optical bandgap sizes of the silver-exchanged metal oxides were small enough for the absorption of lower-energy visible light irradiation. However, under only visible light, photocatalytic activity could not be confirmed because turnover numbers reached only ~0.01 to 0.18 μmol H_2/μmol catalyst before all gas production stopped, as shown in Figure 7c. The loss in visible light activity is related to a decrease in silver content within the interlayer spacing, and the resultant increase of their bandgap sizes, as described below. No gas generation was observed for the silver-exchanged phases under visible light without Pt cocatalysts. Previous work on silver exchange of $RbLaNb_2O_7$ showed that the bandgap size was reduced and

dx.doi.org/10.1021/cs400466b | ACS Catal. 2013, 3, 2547−2555

visible light activity was increased, but photodecomposition of this phase after prolonged irradiation had not been investigated.[9]

Photodecomposition of Silver-Containing Layered Oxides. After photocatalytic testing under UV and visible light irradiation, the PXRD data of the silver-exchanged products revealed the increasing formation of Ag(s), as shown in Figure 8 for $AgLaNb_2O_7$ and $Ag_2La_2Ti_3O_{10}$. The UV−vis DRS data also exhibit an increase in their bandgap sizes into the UV region. Thus, the Ag(I) ions in the interlayer spacing have been photochemically reduced to Ag(s). As a result, the silver content and its contributions to the valence band are reduced, increasing the bandgap size until the layered metal oxide cannot absorb visible light energy.

The photochemical reduction of Ag(I) to Ag(s) within the layered structures produces silver particles at the surface that can greatly influence their photocatalytic activity, similar to Pt cocatalysts. The high electronegativity of Ag(s) compared to the layered perovskite bulk can cause the attraction of photoexcited electrons. The electrons held at these Ag(s) sites, away from concurrently generated holes, inhibit electron−hole recombination.[12,48−51] The silver nanoparticles and 1 wt % Pt cocatalysts on the photocatalyst surface act synergistically to increase the photocatalytic activity; the effect of dual metal cocatalysts (e.g., Pt, Au, Ag, RuO_2) has been previously reported.[50,52−55] However, a large excess of aggregated Ag(s) particles at the surface can also obstruct photon flux and create a larger number of site defects where electron−hole recombination predominates, resulting in lower photocatalytic activity.[12,50,56,57] The layered $Ag_2La_2Ti_3O_{10}$ phase experiences a lower photocatalytic activity after silver exchange given in Table 1 and Figure 7. Further, the Pt-island adhesion deteriorates during photocatalytic measurements, as shown by FESEM in Figure 9. Ohno et al. has shown in previous studies that particles can undergo loss of surface cocatalysts, which hinders electron migration from the metal oxide to the cocatalyst.[46]

CONCLUSIONS

Rubidium-containing layered metal oxides were synthesized by solid-state methods and silver-exchanged by utilization of a low-temperature $AgNO_3$ flux. Irregularly shaped platelet morphologies had an average size of ∼1−5 μm across lateral dimensions. Substituting silver into the interlayer spacing is found to increase the valence band maximum and reduce the bandgap sizes, extending the light absorption into the visible region. Photocatalytic hydrogen formation rates increased after the silver exchange reaction for all layered metal oxides, with the exception of $Ag_2La_2Ti_3O_{10}$. The silver-exchanged $AgA_2Nb_3O_{10}$ layered structures exhibited the highest photocatalytic hydrogen formation rates in aqueous methanol under ultraviolet and visible irradiation (∼13,616 μmol $H_2 \cdot g^{-1} \cdot h^{-1}$) compared to before silver exchange (∼1,418 μmol $H_2 \cdot g^{-1} \cdot h^{-1}$). However, photocatalytic activity under only visible light irradiation is not observed. Electronic-structure calculations based on DFT show the highest-energy valence band states are composed of Ag 4d-orbital and O 2p-orbital contributions within the interlayer spacing of the structure. The lowest-energy conduction-band states arise from the Nb/Ti d-orbital and mixing of O 2p-orbital contributions that are confined to the two-dimensional niobate/titanate sheets within the structure and through which excited-electrons can migrate. The photochemical reduction of Ag(I) to Ag(s) within the layered structures produced silver particles at the surfaces that enhanced photocatalytic activity under UV irradiation, similar to Pt cocatalysts. The silver content and its contributions to the valence band were reduced, increasing the bandgap sizes until the layered metal oxides could not absorb visible light energy.

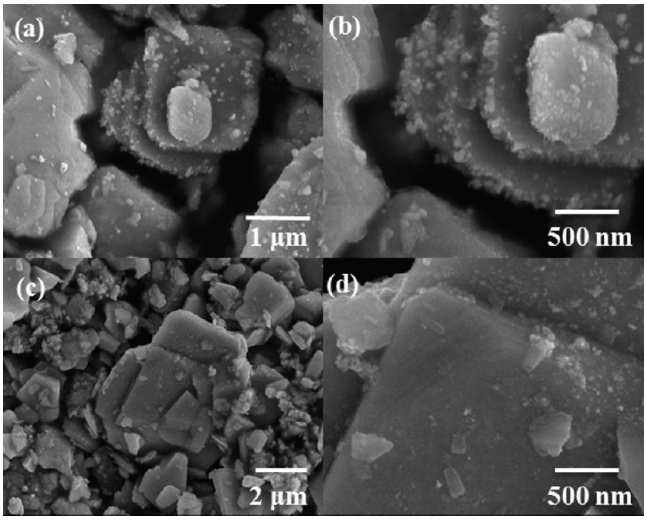

Figure 9. FESEM images of $Ag_2La_2Ti_3O_{10}$ particles with 1 wt % Pt showing nanoislands on the surface (a and b) and after UV phototesting for 6 h (c and d).

ASSOCIATED CONTENT

Supporting Information

Powder X-ray diffraction patterns of all products, table of refined lattice parameters, elemental analysis of silver-exchanged $RbA_2Nb_3O_{10}$ (A = Ca, Sr) products using EDX, powder X-ray diffraction patterns of the silver-exchanged $RbA_2Nb_3O_{10}$ (A = Ca, Sr) products before and after photocatalytic hydrogen generation measurements, UV−vis DRS of all products before and after photocatalytic measurements, and bandgap sizes obtained from UV−vis DRS before and after photocatalytic hydrogen production measurements. This material is available free of charge via the Internet at http://pubs.acs.org.

AUTHOR INFORMATION

Corresponding Author

*E-mail: pamaggar@ncsu.edu.

Notes

The authors declare no competing financial interest.

ACKNOWLEDGMENTS

Support of this research is acknowledged from the Research Corporation for Science Advancement (P.A.M. is a Scialog Awardee). The authors thank C. Mooney (Analytical Instrumentation Facility; NCSU) for SEM images and EDX data.

REFERENCES

(1) Osterloh, F. E. *Chem. Mater.* **2008**, *20*, 35−54.
(2) Lewis, N. S. *Nature* **2001**, *414*, 589−90.
(3) Huang, Y.; Wu, J.; Wei, Y.; Hao, S.; Huang, M.; Lin, J. *Scr. Mater.* **2007**, *57*, 437−440.
(4) Porob, D. G.; Maggard, P. A. *J. Solid State Chem.* **2006**, *179*, 1727−1732.
(5) Fujishima, A.; Honda, K. *Nature* **1972**, *238*, 37−38.

(6) Kato, H.; Asakura, K.; Kudo, A. *J. Am. Chem. Soc.* **2003**, *125*, 3082−9.
(7) Woodhouse, M.; Parkinson, B. A. *Chem. Soc. Rev.* **2009**, *38*, 197−210.
(8) Arney, D.; Hardy, C.; Greve, B.; Maggard, P. A. *J. Photochem. Photobiol., A* **2010**, *214*, 54−60.
(9) Arney, D.; Maggard, P. A. *ACS Catal.* **2012**, *2*, 1711−1717.
(10) Arney, D.; Watkins, T.; Maggard, P. A. *J. Am. Ceram. Soc.* **2011**, *94*, 1483−1489.
(11) Hwang, D. W.; Kim, H. G.; Lee, J. S.; Kim, J.; Li, W.; Oh, S. H. *J. Phys. Chem. B* **2005**, *109*, 2093−102.
(12) Osterloh, F. E. *Chem. Soc. Rev.* **2013**, *42*, 2294−320.
(13) Takata, T.; Shinohara, K. *MRS* **1996**, *454*, 177−185.
(14) Domen, K.; Yoshimura, J.; Sekine, T. *Catal. Lett.* **1990**, *4*, 1−5.
(15) Gopalakrishnan, J.; Bhat, V.; State, S.; Unit, S. C.; Raveau, B.; Cristallographie, L. De *Mater. Res. Bull.* **1987**, *22*, 413−417.
(16) Gopalakrishnan, J.; Bhat, V. *Inorg. Chem.* **1987**, *26*, 4299−4301.
(17) Choi, J.; King, N.; Maggard, P. A. *ACS Nano* **2013**, *7*, 1699−708.
(18) Porob, D. G.; Maggard, P. A. *Chem. Mater.* **2007**, 970−972.
(19) Arney, D.; Porter, B.; Greve, B.; Maggard, P. A. *J. Photochemi. Photobiol., A* **2008**, *199*, 230−235.
(20) Jacobson, A. J.; Lewandowski, J. T.; Johnson, J. W. *Mater. Res. Bull.* **1990**, *25*, 679−686.
(21) Jacobson, A. J.; Johnson, J. W.; Lewandowski, J. T. *Inorg. Chem.* **1985**, *24*, 3727−3729.
(22) Arney, D.; Maggard, P. A. *ACS Catal.* **2012**, *2*, 1−7.
(23) Jacobson, A. *J. Less-Common Met.* **1986**, 116.
(24) Uma, S. *J. Mater. Chem.* **1993**, *3*, 709−713.
(25) Maeda, K.; Mallouk, T. E. *J. Mater. Chem.* **2009**, *19*, 4813.
(26) Wang, B.; Li, C.; Hirabayashi, D.; Suzuki, K. *Int. J. Hydrogen Energy* **2010**, *35*, 3306−3312.
(27) Domen, K.; Kondo, J. *Bull. Chem. Soc. Jpn.* **2000**, *73*, 1307−1331.
(28) Cui, W. Q.; Qi, Y. L.; Cheng, J.; Hu, J. S.; Liang, Y. H. *Adv. Mater. Res.* **2011**, *233−235*, 1646−1649.
(29) Dion, M.; Ganne, M.; Tournoux, M. *Mater. Res. Bull.* **1981**, *16*, 1429−1435.
(30) Thangadurai, V.; Schmid-Beurmann, P.; Weppner, W. *J. Solid State Chem.* **2001**, *158*, 279−289.
(31) Wang, X.; Adhikari, J.; Smith, L. J. *J. Phys. Chem. C* **2009**, 17548−17559.
(32) Geselbracht, M. J.; White, H. K.; Blaine, J. M.; Diaz, M. J.; Hubbs, J. L.; Adelstein, N.; Kurzman, J. A. *Mater. Res. Bull.* **2011**, *46*, 398−406.
(33) Sato, M.; Watanabe, J.; Uematsu, K. *J. Solid State Chem.* **1993**, *107*, 460−470.
(34) Joshi, U. A.; Maggard, P. A. *J. Phys. Chem. Lett.* **2012**, *3*, 1577−1581.
(35) Nakamatsu, H.; Kawai, T. *J. Chem. Soc., Faraday Trans.* **1986**, *82*, 527−531.
(36) Graetzel, M. E. *Energy Resources through Photochemistry and Catalysis*; Academic Press: New York, 1983.
(37) Clark, S. J.; Segall, M. D.; Pickard, C. J.; Hasnip, P. J.; Probert, M. I. J.; Refson, K.; Payne, M. C. *Z. Kristallogr.* **2005**, *220*, 567−570.
(38) Payne, M. C.; Arias, T. a.; Joannopoulos, J. D. *Rev. Mod. Phys* **1992**, *64*, 1045−1097.
(39) Byeon, S.; Nam, H. *Chem. Mater.* **2000**, 1771−1778.
(40) Bhuvanesh, N. S. P.; Woodward, P. M. *J. Am. Chem. Soc.* **2002**, 14294−14295.
(41) Chen, Y.; Zhao, X.; Ma, H.; Ma, S.; Huang, G.; Makita, Y.; Bai, X.; Yang, X. *J. Solid State Chem.* **2008**, *181*, 1684−1694.
(42) Wulfsberg, G. *Inorganic Chemistry*, 1st ed.; University Science Books: Sausalito, 2000.
(43) Zhang, Z.; Yates, J. T. *Chem. Rev.* **2012**, *112*, 5520−51.
(44) Ohtani, B.; Iwai, K.; Nishimoto, S.; Sato, S. *J. Phys. Chem. B* **1997**, *5647*, 3349−3359.
(45) Kraeutler, B.; Bard, A. J. *J. Am. Chem. Soc.* **1978**, *100*, 4317−4318.
(46) Ohno, T.; Bai, L.; Hisatomi, T.; Maeda, K.; Domen, K. *J. Am. Chem. Soc.* **2012**, *134*, 8254−9.
(47) Hwang, D. W.; Lee, J. S.; Li, W.; Oh, S. H. *J. Phys. Chem. B* **2012**, *7*, 4963−4970.
(48) Hermann, J. M.; Disdier, J.; Pichat, P. *J. Phys. Chem.* **1986**, *90*, 6028−6034.
(49) Henglein, A. *J. Phys. Chem.* **1979**, *83*, 2209−2216.
(50) Kundu, S.; Kafizas, A.; Hyett, G.; Mills, A.; Darr, J. A.; Parkin, I. P. *J. Mater. Chem.* **2011**, *21*, 6854.
(51) Zhao, W.; Chen, C.; Li, X.; Zhao, J.; Serpone, N. *J. Phys. Chem. B* **2002**, *106*, 5022−5028.
(52) Kafizas, A.; Kellici, S.; Darr, J. A.; Parkin, I. P. *J. Photochem. Photobiol., A* **2009**, *204*, 183−190.
(53) Xiong, A.; Yoshinaga, T.; Ikeda, T.; Takashima, M.; Hisatomi, T.; Maeda, K.; Setoyama, T.; Teranishi, T.; Domen, K. *Eur. J. Inorg. Chem.* **2013**, DOI: 10.1002/ejic.201300439.
(54) Yang, J.; Wang, D.; Han, H.; Li, C. *Acc. Chem. Res.* **2013**, *46*, 1900−1909.
(55) Tanaka, A.; Sakaguchi, S.; Hashimoto, K.; Kominami, H. *ACS Catal.* **2013**, *3*, 79−85.
(56) Hu, X.; Hu, C.; Qu, J. *Mater. Res. Bull.* **2008**, *43*, 2986−2997.
(57) Kudo, A.; Miseki, Y. *Chem. Soc. Rev.* **2009**, *38*, 253−278.